Ultrasound in Medicine & Biology 000 (2025) 1−15

Contents lists available at ScienceDirect

Ultrasound in Medicine & Biology

journal homepage: www.elsevier.com/locate/ultrasmedbio

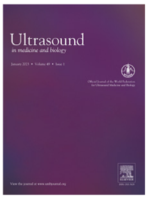

Original Contribution

Assessment of Spatially-Varying Arterial Wall Stiffness and Pressure Using a Physics-Informed Neural Network and Pulse Wave Imaging: An *in Silico* and Experimental Phantom Study of Stenotic Vessels

Tuhin Roy [a], Paul Kemper [a], Nima Mobadersany [a], Haokang Shi [a], Elisa E. Konofagou [a,b,c,*]

[a] *Department of Biomedical Engineering, Columbia University, New York City, USA*
[b] *Department of Radiology, Columbia University, New York City, USA*
[c] *Department of Neurological Surgery, Columbia University, New York City, USA*

ARTICLE INFO

Key Words:
Pulse wave propagation
Arterial compliance
Inverse problem
Physics-based machine learning

ABSTRACT

Objective: Arterial stiffness is a key predictor of cardiovascular mortality. This study utilizes a physics-informed neural network (PINN) model to estimate spatially varying arterial stiffness by leveraging ultrasound-based Pulse Wave Imaging (PWI) and Vector Flow Imaging (VFI).

Methods: The PWI and VFI frameworks provide high-frame-rate wall displacement and blood flow velocity data, which are incorporated into a PINN constrained by linearized 1D differential equations modeling pulse wave propagation in heterogeneous vessels. The model was validated using *in-silico* simulations and physical plaque phantoms.

Results: The proposed PINN model effectively captured variations in localized compliance, which is indicative of arterial wall stiffness, in both *in-silico* and phantom experiments, and remained robust under varying inlet and outlet boundary conditions. Notably, incorporating flow velocity data enhanced reconstruction accuracy by 13.84% over displacement-only methods. The approach yielded low bias in homogeneous cases (1.41%), with higher biases for stiffer (3.95%) and softer (8.10%) plaque scenarios, mainly due to limitations in the 1D modeling and lack of explicit boundary condition integration.

Conclusion: The findings presented herein indicate the PINN framework has strong potential for non-invasive assessment of focal arterial stiffness, such as in atherosclerotic plaques. Future work aims to include nonlinear vascular dynamics and extend the model to 2D or 3D to better capture complex blood flow behavior seen in stenotic arteries.

Introduction

Cardiovascular diseases (CVDs) are a leading cause of global mortality, with arterial stiffness serving as a predictor of cardiovascular events and enhancing diagnostic accuracy, particularly in assessing the carotid artery's mechanical properties. Given its accessibility and clinical relevance because of the part of the central arterial system, understanding localized stiffness variations in the carotid artery is essential for early diagnosis and management of cardiovascular conditions [1,2]. Among the parameters used to assess arterial stiffness, Pulse Wave Velocity (PWV) is widely recognized for its robustness and reliability [3].

Applanation tonometry is a technique that measures pulse pressure at two temporally synchronized locations, typically the femoral and carotid arteries. By analyzing the time delay and distance between these sites, the average PWV can be estimated [4]. Additionally, empirically derived transfer functions are employed to compare pressure waveforms recorded at different anatomical sites [5]. These global estimates of PWV have become a standard clinical indicator of arterial stiffness, utilized in a variety of medical applications. However, common vascular pathologies, such as atherosclerotic plaques and abdominal aortic aneurysms (AAAs), cause focal changes in vessel properties, making localized estimation of vascular wall elastic properties crucial for accurate disease characterization [6,7]. Improved estimation of spatially varying arterial properties can enhance predictions of rupture risks, potentially reducing unnecessary surgeries in stable cases and ensuring timely interventions for vulnerable cases.

To characterize rupture risk, magnetic resonance imaging (MRI) is currently considered the gold standard for assessing carotid plaque vulnerability due to its high sensitivity in detecting histological features associated with vulnerability. However, its application is limited by time constraints, contraindications, and costs [8], as well as a maximum *in vivo* resolution of 0.7 mm (isotropic) when using

---

* Corresponding author. Department of Biomedical Engineering, Columbia University, New York City, USA.
E-mail address: ek2191@columbia.edu (E.E. Konofagou).

https://doi.org/10.1016/j.ultrasmedbio.2025.09.012
Received 24 December 2024; Revised 15 August 2025; Accepted 13 September 2025

0301-5629/Published by Elsevier Inc. on behalf of World Federation for Ultrasound in Medicine and Biology.

dedicated coils [9]. Recent advancements have also highlighted the integration of photoplethysmography (PPG) for assessing arterial stiffness metrics [10,11]. While PPG provides reliable information on vascular function, particularly regarding blood flow at the peripheral arteries, its effectiveness is limited by its shallow penetration depth for the central arteries.

In contrast, ultrasound is a reliable plaque detection technique for evaluating stenosis degree, plaque morphology, and it is already widely used in stroke risk assessment [8]. Additionally, ultrasound offers at least twice the resolution of MRI. Recently, emerging ultrasound techniques have been developed to directly assess the mechanical properties (stiffness) of plaques in addition to their morphological features. Among these techniques, shear wave elastography [12,13] excites the arterial wall by applying an external mechanical force, either through acoustic radiation force (ARF) or an external vibrator, and subsequently tracks shear wave speed to compute arterial stiffness. While effective for straight arteries [14,15], shear wave elastography faces challenges in stenotic cases particularly in the stiffer plaques due to the reduction of displacement amplitude leading to low signal-to-noise ratio to track shear wave propagation when interacting with plaques of higher stiffness [16−18]. To address this challenge, researchers have explored on-axis ARF-based approaches, such as Acoustic Radiation Force Impulse (ARFI), specifically for carotid atherosclerosis plaques [19]. Additionally, there are strain-based ultrasound measurement techniques that employ strain elastograms, homodyned-K, and Nakagami parameter maps to detect regions of fibrous tissue, lipid, and calcification [20]. In addition to the non-invasive ultrasound techniques, there are intravascular ultrasound (IVUS) approaches to vascular strain imaging that offers much higher spatial resolution, albeit at the cost of invasiveness and have been used to measure differential strain exhibited by various plaque components, aiding in the identification of fibrous, lipid, and calcified regions [21−23].

In contrast, pulse wave imaging (PWI), noninvasively estimates vascular wall motion induced by the natural pulsatile motion of the artery resulting from blood flow [24−30]. Recent studies on experimental phantoms [31,32] have demonstrated that changes in pulse wave velocity can effectively differentiate between various stiffness constituents of plaques. Additionally, a 2D cross-correlation approach in vector flow imaging (VFI) was pioneered and reported by employing RF-based flow estimation with SVD filtering to provide blood flow patterns and the respective arterial characteristics [33,34].

In recent years, while there have been efforts applying inverse problem approaches towards improving ultrasound imaging-based approaches [35−39], there have been studies applying Inverse Problem to estimating the mechanical properties of the underlying soft tissues that can be found in a review article which highlights various cases, ranging from bulk tissues such as the liver and breast to vascular phantoms mimicking coronary arteries [40]. One such approach is the pulse wave inverse problem (PWIP) [41] which estimates the arterial wall compliance by fitting a computational model of pulse wave propagation to the measured data of wall motion. While there is an analytical expression (Moens-Korteweg equation [42]) to link arterial stiffness (inverse of compliance) and the pulse wave velocity for straight homogenous artery that yields a single value of arterial compliance over a cardiac cycle, the PWIP approach circumvents the assumptions inherent in this model. Instead, it iteratively adjusts the estimated displacement from the model to align with the measured displacement, thereby generating a compliance map across the entire lateral length of the ultrasound transducer as opposed to a single value obtained with the analytical approach. This is particularly useful in complex heterogeneous cases, such as stenotic arteries, where assumptions such as wall homogeneity across lateral length become invalid. Furthermore, by integrating the VFI framework, we can incorporate the flow estimation into the PWIP approach, thereby correcting compliance estimates for both anatomical and flow effects. While arterial wall motion and flow velocity can serve as independent imaging biomarkers, they are inter-dependent and affected by boundary conditions. In contrast, arterial compliance is intrinsically linked to mechanical properties and remains independent of geometry and boundary conditions. Therefore, by utilizing both wall motion and flow velocity together in an inverse problem framework to estimate arterial wall compliance, outliers are less likely than when considering only wall motion. The PWIP has previously been shown to be robust against reflections, whereas wave-based tracker (pulse wave velocity) might be impacted [41]. This remains the case when flow is included, which is particularly beneficial in cases with significant reflections, such in the case of stenosis. One way to solve this complex problem is use of a 3D fluid-structure interaction (FSI) model, such as the coupled Eulerian-Lagrangian method [43]. However, obtaining a single solution from these 3D FSI models is far more computationally costly, rendering them impractical for inverse problem approaches [41,44].

To address this, one of our previous studies [41] has utilized one-dimensional (1D) pulse wave propagation equations within a finite-difference-based framework and a gradient-based optimization setting for the inverse problem. This method, however, requires precise knowledge of the inlet and outlet boundary conditions, as it solves the governing differential equations in the conventional manner. Recently, a physics-informed neural network (PINN) based inverse model has been used by our group [45,46], which integrates both PWI and VFI-measured wall displacement and fluid flow measurements. The feasibility of this model has been investigated using PWI and VFI measurements in swine and humans for homogenous cases with straight geometry. A similar PINN-based model has been utilized in [47] to estimate both pressure and compliance for the straight and homogenous arteries and verified the framework with findings from the FIELD-II simulations. However, the PINN model presented in this work considered spatially down-sampled data by a factor of 8 to address the GPU-memory constraint leading to coarser lateral resolution. This limitation is particularly critical when analyzing stenotic arteries, where significant changes in wall motion and flow velocity occur within the plaque region. Such coarse lateral resolution is insufficient to accurately capture these localized variations, especially when the plaque length is in the order of 10 mm.

In this work, we extended the PINN model proposed by [45−47] to the cases of stenotic arteries with varying plaque stiffness and length for localized compliance assessment. We also demonstrated the robustness of the PINN model in addressing unknown inlet and outlet boundary conditions, as well as its effectiveness when utilizing only wall motion data compared to scenarios where both wall motion and flow velocity data are considered. The feasibility of the model was validated through both *in silico* simulations and phantom experiment data. Note that this work built upon a study presented at the IEEE 2024 Ultrasonics, Ferroelectrics, and Frequency Control Joint Symposium (UFFC-JS) [48].

Materials and methods

Pulse wave inverse problem

The pulse wave inverse problem (PWIP) is an approach designed to recover unknown vessel properties by fitting parameters from a computational model to measured data using optimization methods. In this context, the computational model consists of linearized partial differential equations governing one-dimensional pulse wave propagation in heterogeneous flexible tubes [41], under the assumption that fluid velocity is much smaller than pulse wave velocity:

$$k_p \frac{dP}{dt} + A\frac{du}{dx} = 0 \tag{1}$$

$$\frac{du}{dt} + \frac{1}{\rho}\frac{dP}{dx} + K_R u = 0 \tag{2}$$

where P is the fluid pressure, u is the fluid velocity, x is the coordinate along the vessel, t is time, A is the cross-sectional area of the tube, ρ is the fluid density, and K_R is the viscous resistance per unit length of the tube. k_p represents the local vessel compliance. Assuming that the inertial and viscous forces ($K_R u$) in the vessel wall are negligible (a reasonable assumption for larger vessels [49]), the cross-sectional area (A) of the vessel depends linearly on the pressure alone:

$$A = A_0 + k_p(P - P_0) \tag{3}$$

where A_0 is the vessel area at the reference pressure, P_0. The equation (3) is the Bramwell Hill equation, which computes the compliance from the ratio of the changes of cross-sectional area to changes to pressure,

$$k_p = \Delta A / \Delta P \tag{4}$$

where, ΔA, ΔP represent the changes in the lumen area and pressure respectively. Among various approaches to solving differential equations, one approach is to use an implicit 4-point primitive finite difference method to solve for $u(x,t)$ and $P(x,t)$ over discretized spatial (x), and temporal (t) dimensions for the above equations. The detailed computational model solving equations (1) to (3) is described in one of our earlier studies in [41].

In the context of the inverse problem, we have direct PWI measurement inputs, more specifically, arterial wall motion and blood flow velocity, along with assumptions on the underlying physics. The objective of the inverse problem is to estimate the unknown compliance of the arterial wall. In our previous work [41], we employed a gradient-based optimization technique to address this inverse problem, solving the forward problem (or governing equations) using finite-difference methods at each iteration of the optimization process. However, this approach necessitates knowledge of the inlet and outlet boundary conditions and can be sensitive to measurement noise. Recently, several data science-based approaches have emerged for solving inverse problems, among which the PINN stands out. PINNs allow for solving the underlying differential equations without requiring boundary condition knowledge and are more robust in the presence of measurement noise, as the neural networks learn from the measured data. In the following section, we describe the PINN model utilized in this study.

Physics-informed neural network

To address the inverse problem, we employ a PINN approach [46], where the solution of partial differential equations (PDEs) is parameterized by a neural network (NN), and the physics (residual of the PDEs) is included in the cost function. We utilize a multiscale Fourier network architecture, which is well-suited for multiscale problems such as pulse wave propagation, characterized by higher frequency content in the time dimension (t) compared to the position dimension (x). The neural network consists of three layers with 64 units each and uses tanh activations. The Fourier mapping scale is set to 1 and 5 for time and 1 for space. Figure 1 illustrates the structure of the PINN used in this study.

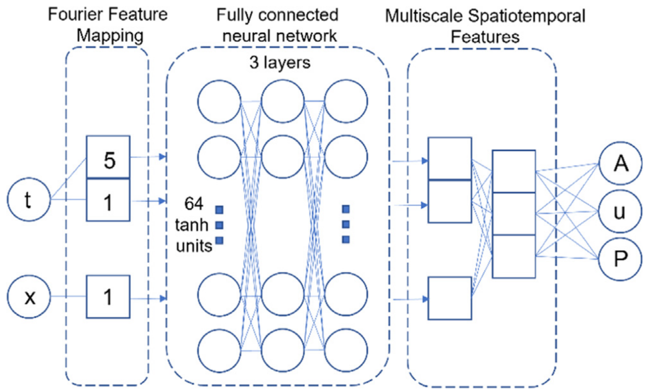

Figure 1. A schematic of the considered neural network structure in the proposed PINN model is shown here. The neural network structure consists of input layer of space and time points, Fourier Feature Mapping layer, fully connected 3 layers with 64 neurons and tanh activation function, multiscale spatiotemporal feature layer followed by the output layer of lumen area, flow velocity, and pressure.

Nondimensionalization is performed to ensure that the terms in the cost function are of the same order of magnitude. The characteristic variable for length is chosen to be the square root of the mean cross-sectional area of the vessel, and the velocity is normalized by its peak value across the measured field of view. Inputs are normalized to have zero mean and unit variance to enhance the robustness of neural network training via back-propagation. The PDEs are included as an error term, with derivative terms calculated using automatic differentiation. Consequently, the total loss function, L_{total}, consists of the residual from the PDE term L_{PDE}, and the data misfit term L_{Data}:

$$L_{total} = w_{Data}L_{Data} + w_{PDE}L_{PDE};\ L_{Data} = \sum \frac{\| NN(\theta; x; t) - (A; u) \|^2}{N_x N_t}; \tag{5}$$

$$L_{PDE} = \sum \frac{\| k_p \frac{dP}{dt} + A\frac{du}{dx} \|^2 + \| \frac{du}{dt} + \frac{1}{\rho}\frac{dP}{dx} \|^2}{N_x N_t} \tag{6}$$

where N_x and N_t are the number of spatial and temporal samples, respectively. The weights w_{Data} and w_{PDE} are associated with the data loss and PDE loss terms. In this work, these weights are kept constant at 0.04 and 100, respectively, consistent with the numerical order of each term in the loss function. While we verified that the results do not change significantly with variations in the weight terms, future work will involve optimizing these weights.

With respect to the training data size, because of the considered GPU (Quadro RTX 5000) memory constraints (approximately 16 GB RAM on GPU), we reduced the dataset, specifically in the time dimension by focusing on one complete cycle of data yielding a dimension of less than $8333/3 = 2778$ (based on a pulse repetition frequency of 8333 Hz and three-angle compounding), and in the spatial dimension all the 128 elements data of the L7-4 transducer considered in our PWI + VFI framework that we use for clinical, *in vivo* studies in human subjects. It is important to note that we utilized the GPU in its full capacity by considering the latest TensorFlow module optimized for this GPU. This approach yields a typical training data size of (128 × 2778) for both wall motion and flow velocity matrices, where the first dimension represents the lateral spatial direction, and the second dimension corresponds to time. Here note that this study considers the 1D version of the governing equations, so both wall and flow velocity data are along the length of the artery (lateral direction) and the flow velocity matrix reflects the peak systolic velocity occurring at the centerline of the lumen over time.

In the optimization process, the wall compliance (k_p) is optimized along with the weights and biases (θ) of the neural network. Optimization is performed using the Adam optimizer with a learning rate of 0.001, a decay rate of 0.8, and a fixed iteration of 20,000. While these parameters were selected based on our previous studies in [45,46], we plan to conduct a comprehensive analysis of their effects on the proposed PINN model in future research.

Simulations for in-silico *data*

The numerical implementation of the 1-D wave propagation PDEs (equations [1] to [3]) was utilized to generate three forward simulations corresponding to three cases: (1) homogeneous, (2) stiffer plaque, and (3) softer plaque. The Young's modulus values for these cases are shown in Figure 2a. A raised cosine smoothing was applied to ensure a smooth transition from a nominal Young's modulus of 160 kPa to a maximum of 320 kPa for the stiffer plaque and 80 kPa for the softer plaque cases. The selection of the base Young's modulus at 160 kPa is based on our earlier findings of the pulse wave velocity (PWV) of approximately 5 m/s in the non-healthy study cohorts [50] and then back-calculating the Young's modulus (E) from the Moens-Korteweg equation, $PWV = \sqrt{E.h/2r\rho(1-\nu^2)}$, where, typical wall thickness (h) is

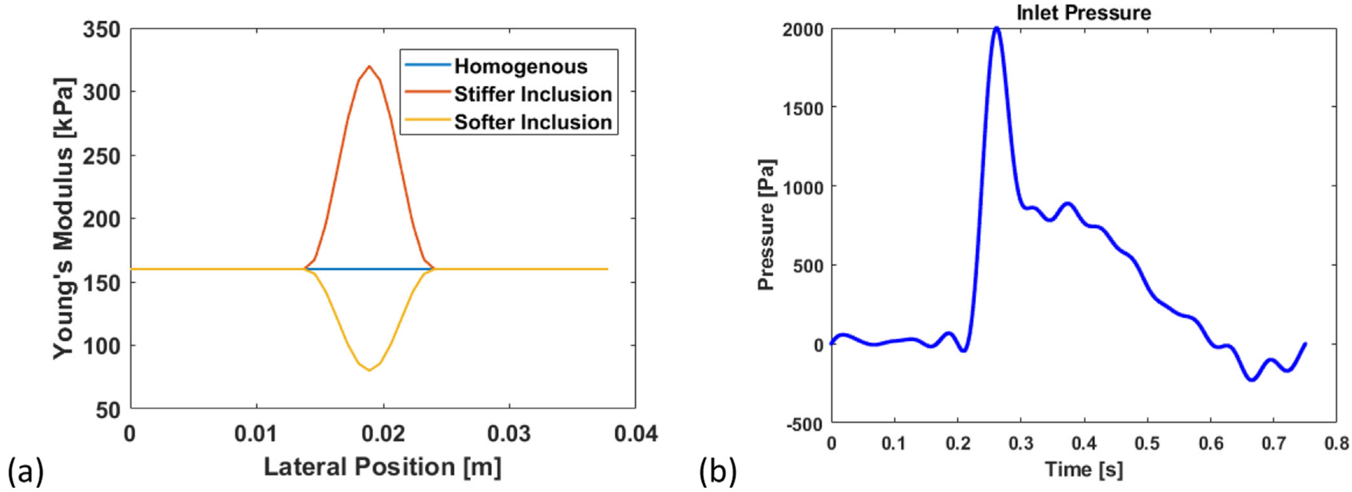

Figure 2. The input Young’s modulus (a) and the inlet pressure boundary condition (b) for the 1-D pulse wave propagation simulation are presented here. The blue, red, and yellow colors in (a) show the considered Young’s modulus distribution in the in silico homogenous, stiffer plaque and softer plaque cases respectively.

approximately 0.75 mm, lumen radius (r) is approximately 3 mm, the blood density (ρ) is 1060 kg/m^3, and the Poisson’s ratio (ν) is 0.5 for the soft tissues. Regarding the Young’s modulus of the plaque, literature presents a broad range of values [51]. In this study, we considered not only 320 kPa for the stiffer plaque and 80 kPa for the softer plaque, but also 750 kPa and 40 kPa for the stiffer and softer plaques, respectively (see Fig. 16, Fig. 17). With respect to the boundary conditions, an inlet pressure boundary condition shown in Figure 2b, and an outlet resistance boundary condition of R = 1.e-4 $ms^{-1}Pa^{-1}$ were applied to solve the governing equations. The inlet pressure boundary condition used in this simulation study is derived from pulse pressure measurements obtained by our clinical ultrasound setup from a healthy subject, while the outlet resistance boundary condition is based on observations reported previously [41]. The problem domain considered a representative length of 40 mm and a total time of 0.75 seconds. The reference compliance against which the estimated compliance from the PINN model is assessed was computed using the Bramwell Hill model (equation (4)) on the simulated data.

Phantom experiments

For the phantom experiment, we used in-house made polyvinyl alcohol (PVA) based arterial mimicking phantoms. Following the steps outlined in [32], we constructed three phantoms: (1) a straight vessel (no plaque), (2) a stenotic vessel with stiffer plaque, and (3) a stenotic vessel with softer plaque. The stenotic vessels have a 63% degree of stenosis, representing the maximum percentage of the arterial wall inner diameter occluded by the stenosis. The straight phantom underwent six freeze-thaw cycles. For the stenotic vessel with a stiffer plaque, the plaque was first generated through six freeze-thaw cycles. This plaque was then placed inside another mold, and additional PVA material was poured around it. The entire setup underwent an additional six freeze-thaw cycles to create the stenotic vessel with stiffer plaque. In the case of the softer plaque, the phantom wall was initially generated through four freeze-thaw cycles, followed by pouring PVA material only for the plaque. This complete setup then underwent an additional two freeze-thaw cycles to form the stenotic vessel with softer plaque. The corresponding B-mode images are shown in Figure 5. Additionally, we investigated the effect of ultrasound scatterers in the surrounding tissue for the straight phantoms by incorporating graphite (6% of the total volume) within the gelatin mix used to mimic the surrounding tissue of the human common carotid artery. Finally, mechanical testing, that is, uniaxial compressive test using Instron 5866 machine (Instron Corporation, Norwood, MA, USA) along with Bluehill Universal software v3.0 was performed to check the stiffness estimate of each of the considered cases (for straight part of the stenotic phantom: $E_0 = 30$ kPa; for plaque specimen in stiffer plaque phantom: $E_0 = 95$ kPa; for plaque specimen in softer plaque phantom: $E_0 = 12$ kPa) details of which are available in [32].

Figure 3 shows a schematic of the phantom setup considered in this study. A computer-controlled displacement pump (CompuFlow 1000, Shelley Medical Imaging Technologies, Toronto, Canada) was connected to both the inlet and outlet of the phantom to circulate a blood-mimicking fluid (Doppler Fluid, Model 769DF, CIRS, Norfolk, VA, USA). The pump generated physiological pulsatile flow with a waveform resembling that of the common carotid artery [52], with an amplitude of 10 mL/s. The total duration of each pump cycle was set to 1.9 seconds, comprising 0.9 seconds of a common carotid artery flow waveform followed by a 1-second interval. This interval allows for the attenuation of reflections from the previous cycle, effectively eliminating the influence of reflected waves on the forward wave of the new cycle. The propagation of the pulse wave and blood flow was monitored throughout the phantom using PWI and VFI techniques, which are described in the following section.

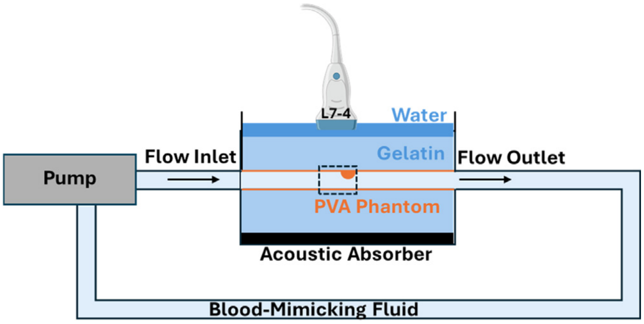

Figure 3. This schematic illustrates the phantom experiment setup utilized in this study. A peristaltic flow pump generates the flow of Doppler fluid through the phantom lumen. The phantom is encased in gelatin, simulating the surrounding tissue of the common carotid artery. An acoustic absorber is positioned at the bottom of the phantom setup to eliminate any ultrasound reflections from the base. Additionally, we limited our experimental observations to the prestenotic region, as the assumptions of the underlying model are significantly violated in the post-stenotic region due to the presence of turbulence and other related factors (see the Discussion section for further details).

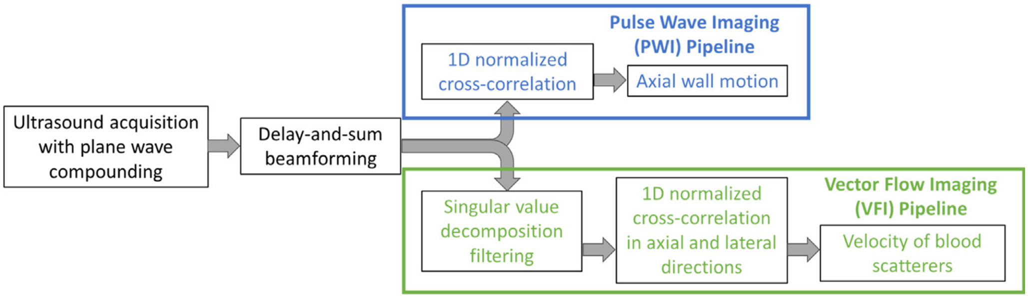

Figure 4. A flowchart of the Pulse Wave Imaging (PWI) and Vector Flow Imaging (VFI) pipeline is shown here. The process consists of the following steps: (1) Ultrasound acquisition with plane wave coherent compounding with 3 angles and Delay-and-sum (DAS) beamforming are applied. (2) In the pulse wave imaging pipeline, subsequently GPU-based 1D normalized cross-correlation is applied on the manually segmented top and bottom walls to get the axial wall velocity. (3) In the VFI pipeline, a singular value decomposition filter is applied to separate out the wall motion first followed by the 1D normalized cross-correlation in both axial and lateral directions to get the velocity of the blood flow. Together the wall and flow velocities will be used in the proposed framework to estimate the underlying material properties of the arterial wall.

Pulse wave and VFI

A flowchart of the PWI and VFI setup is illustrated in Figure 4. In the PWI pipeline, high frame rate (3 kHz) ultrasound channel data are acquired using a 128-element L7-4 linear array (Philips Healthcare, Andover, MA, USA) operating at a center frequency (Fc) of 5.2 MHz, with a bandwidth of 4-7 MHz (58%), in conjunction with a Vantage 256 research ultrasound system (Verasonics, Seattle, Washington, United States) with a pulse repetition frequency of 8333 Hz. To ensure sufficient image quality and maintain a high frame rate, coherent compounding with three plane wave angles (-2°, 0°, 2°) is employed according to [53]. Delay-and-sum (DAS) beamforming is applied to the acquired channel data to produce full radiofrequency (RF) frame sequences [53]. A sub-sample GPU-based 1D normalized cross-correlation algorithm is then used to obtain displacement values. The carotid wall is manually segmented to extract the axial wall velocities of each wall. To eliminate potential rigid motion, the velocity at the bottom wall is subtracted from the velocity at the top wall. Linear regression is employed to calculate the slope of the peak wall acceleration, which is the estimation of the pulse wave velocity (PWV) [54].

In the VFI framework, blood flow is estimated by tracking the 2D motion of blood scatterers using speckle tracking [34]. Singular value decomposition (SVD) is performed to eliminate the slow motion of the arterial wall [55]. Subsequently, a 1D normalized cross-correlation kernel is applied to consecutive filtered RF frames in a 2D search. This is done using a kernel size of 1.4784 mm with an overlap of 1 axial sample (0.01848 mm) to estimate the inter-frame displacements of the blood scatterers. The resulting inter-frame displacements are then normalized by the frame rate to obtain the axial and lateral flow velocity components.

Convergence metrics

To ensure the convergence of the proposed PINN model, the resulting wall motion and flow velocity from the PINN model were compared with the corresponding actual values for both simulated and phantom cases. The normalized difference was computed using the following equation (7). This comparison helps validate the accuracy and robustness of the PINN model in estimating the desired parameters.

$$\textit{Normalized difference} = \frac{\textit{PINN output} - \textit{Reference value}}{\|\textit{Reference value}\|_2} \tag{7}$$

To compare the estimated compliance ($k_p^{estimated}$) with the reference value (k_p^{ref}) in the *in silico* study, we calculated the percentage bias using,

$$bias = \frac{\|k_p^{estimated}(x) - k_p^{ref}(x)\|}{\|k_p^{ref}(x)\|} \times 100 \tag{8}$$

Results

In silico experiments

Figure 6 (a and b) illustrates the wall motion and flow velocity for the straight homogeneous case from the 1D simulation. The corresponding outputs from the PINN model are presented in Figure 6 (c and d), respectively. The normalized differences between the PINN model results and the 1D simulation results are shown in Figure 6 (e and f) for wall motion and flow velocity, respectively. There is a strong agreement between the PINN results and the actual 1D simulation results, with a maximum difference of 0.03% and 0.04% for wall motion and flow velocity respectively in the region of interest (marked by red colored

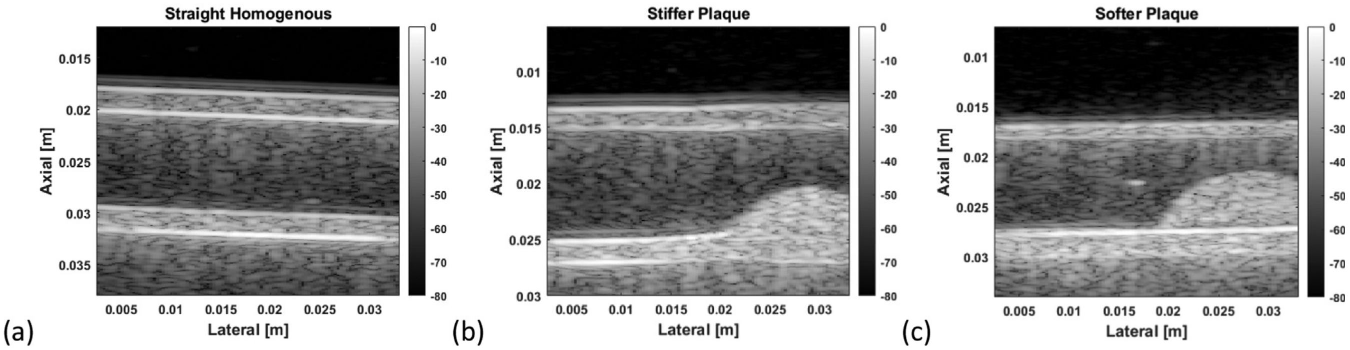

Figure 5. B-mode images of the phantoms of (a) straight homogenous, (b) stiffer plaque, and (c) softer plaque compared to the wall material are shown here. We limited our experimental observations to the pre-stenotic region, as the assumptions of the underlying model are significantly violated in the post-stenotic region due to the presence of turbulence and other related factors (see the Discussion section for further details).

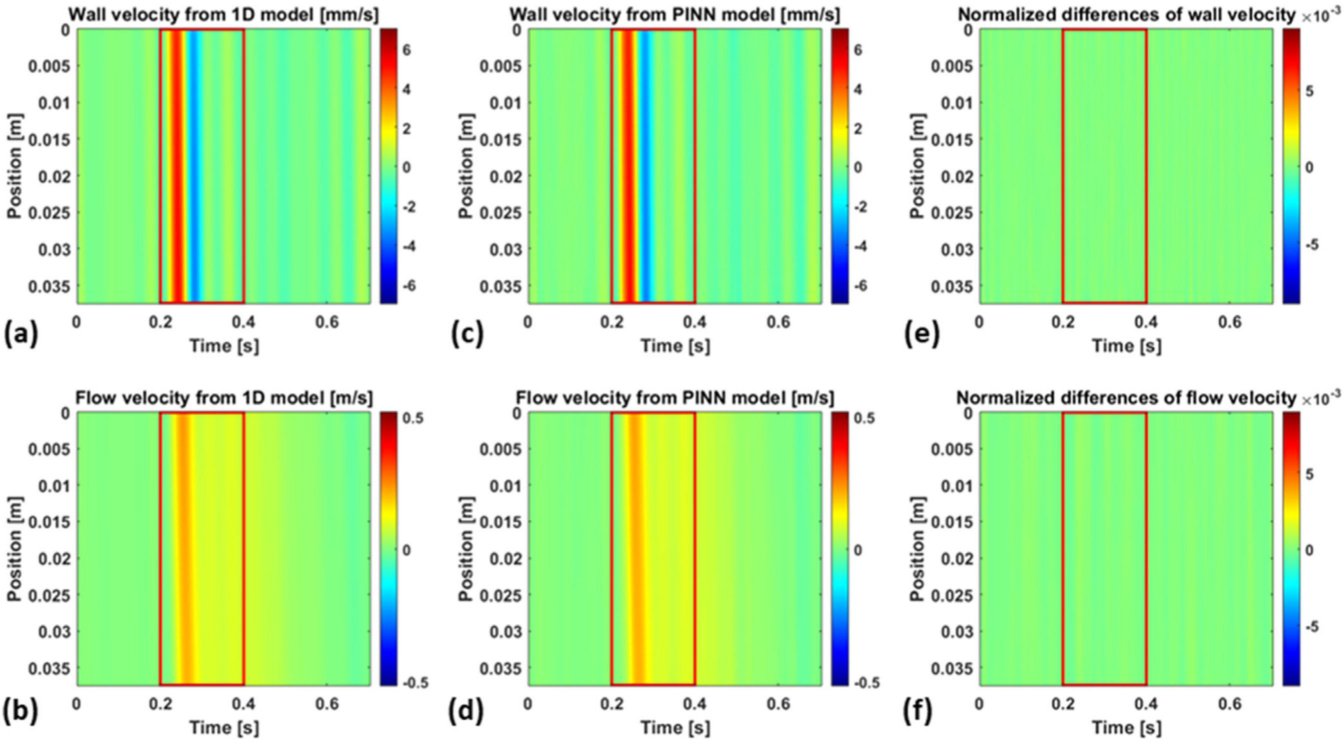

Figure 6. In-silico wall motion and flow velocity for the homogeneous case are shown in (a) and (b), respectively. The corresponding PINN outputs are displayed in (c) and (d). The normalized differences between the in-silico data and the PINN outputs are presented in (e) and (f). The region of interest (marked with a red box) is chosen based on the location of the propagating wave. The maximum differences in the region of interest for wall velocity and flow velocity are 0.03% and 0.04% respectively.

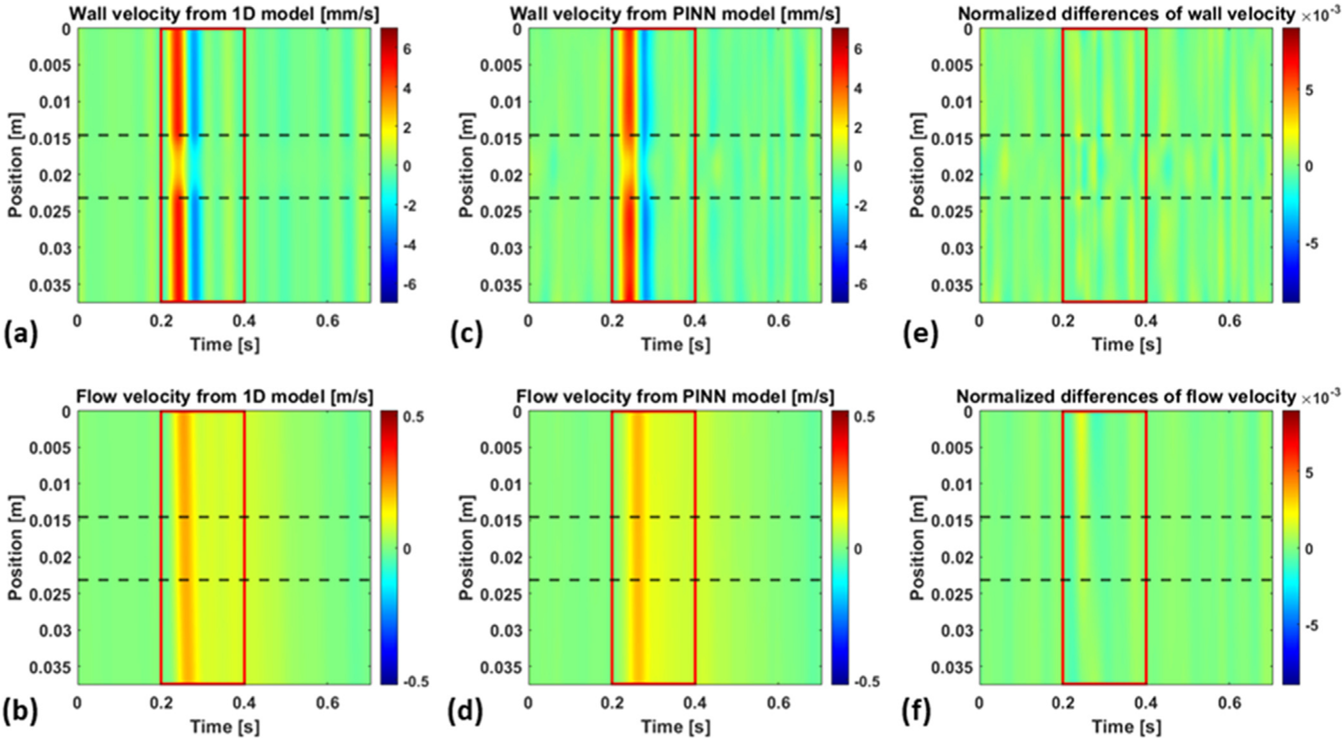

Figure 7. In-silico wall motion and flow velocity for the stiffer plaque case are shown in (a) and (b), respectively. The corresponding PINN outputs are displayed in (c) and (d). The normalized differences between the in-silico data and the PINN outputs are presented in (e) and (f). The region of interest (marked with a red box) is chosen based on the location of the propagating wave. The maximum differences in the region of interest for wall velocity and flow velocity are 0.13% and 0.18% respectively. The area between the black dashed lines indicates the region where wall stiffening occurred.

box in Fig. 6). The region of interest was chosen based on the location of the primary propagating wave.

Similar analyses were performed for the 1D model with a stiffer plaque, as described in the Materials and Methods section. The wall motion and flow velocity for this case are presented in Figure 7 (a and b), with the corresponding outputs from the PINN model shown in Figure 7 (c and d). The normalized differences are depicted in Figure 7 (e and f) for wall motion and flow velocity, respectively. The match between the PINN model and the 1D simulation results is well within the acceptable limit, with a maximum difference of 0.13% and 0.18% respectively for the wall motion and flow velocity in the region of interest.

For the 1D model with a softer plaque, the wall motion and flow velocity are shown in Figure 8 (a and b), while the corresponding outputs from the PINN model are presented in Figure 8 (c and d). The normalized differences for these quantities are shown in Figure 8 (e and f), respectively. Similarly, the agreement is deemed good with a maximum difference of 0.12% and 0.11% respectively for the wall motion and flow velocity in the region of interest. These results demonstrate the accuracy and robustness of the PINN model in estimating wall motion and flow velocity across different cases, including homogeneous, stiffer plaque, and softer plaque scenarios.

Subsequently, from the output area and pressure of the PINN model, the compliance of the arterial wall and hence the pulse wave velocity were obtained using the generalized linear pressure (P) − area (A) relationship (equation [4]). The variations in compliance, and the estimated lumen pressure and PWV for the three cases mentioned earlier are shown in Figure 9 and Figure 10, respectively.

As expected, the compliance remained constant for the homogeneous case (Fig. 9a), decreased in the middle section for the stiffer plaque (Fig. 9b), and increased in the middle section for the softer plaque (Fig. 9c). However, there was a consistent bias (1.41% for the homogenous case, 3.95% for the stiffer plaque, and 8.10% for the softer plaque cases) in the resulting compliance compared to the reference value. Correspondingly, the estimated PWV was constant for the homogeneous case, higher in the middle section for the stiffer plaque, and lower in the middle section for the softer plaque (Fig. 10b). Additionally, the luminal pressure over the cardiac cycle at the inlet (at the start of the transducer lateral location) corresponding to the above considered three cases are shown in Figure 10a. In the *in-silico* cases, the considered inlet pressure (Fig. 2b) used to generate the *in-silico* data were considered as the reference to verify the PINN-estimated lumen pressure results as shown in Figure 10a. In all the three considered cases, the estimated lumen pressure was close to the reference value. The loss histories for these three cases are presented in Figure 11, demonstrating the convergence and stability of the PINN model during the training process.

Figure 12 illustrates the variation in compliance for the homogeneous case, comparing scenarios in which flow velocity was either included or excluded from the analysis. The inclusion of flow data resulted in a 13.84% increase in accuracy compared to the case without the flow data. Both sets of results were compared against the reference compliance value, highlighting the effectiveness of incorporating both wall motion and flow velocity data for more accurate compliance estimation.

Figure 13 presents the results corresponding to the effect of the inlet pressure boundary condition. In this study, we considered three inlet pressures with maximum values of 2, 10, and 20 kPa, as shown in Figure 13a. The corresponding estimated lumen pressure at the inlet along with the reference value (inlet pressure used to generate the *in-silico* data), loss history and the estimated compliance from the proposed PINN model are depicted in Figure 13 (a to c), respectively. These results highlight the model's robustness and accuracy under varying inlet pressure conditions. However, a bias of approximately 10^{-10} m^2/Pa (less than 10%) was observed when compared to the reference compliance, as indicated in Figure 15a.

Figure 14 (a and b) show the loss history and compliance variation results for three different values of resistance boundary condition at the outlet. This analysis demonstrates the effect of the outlet boundary condition on the proposed model. The results confirmed that the PINN

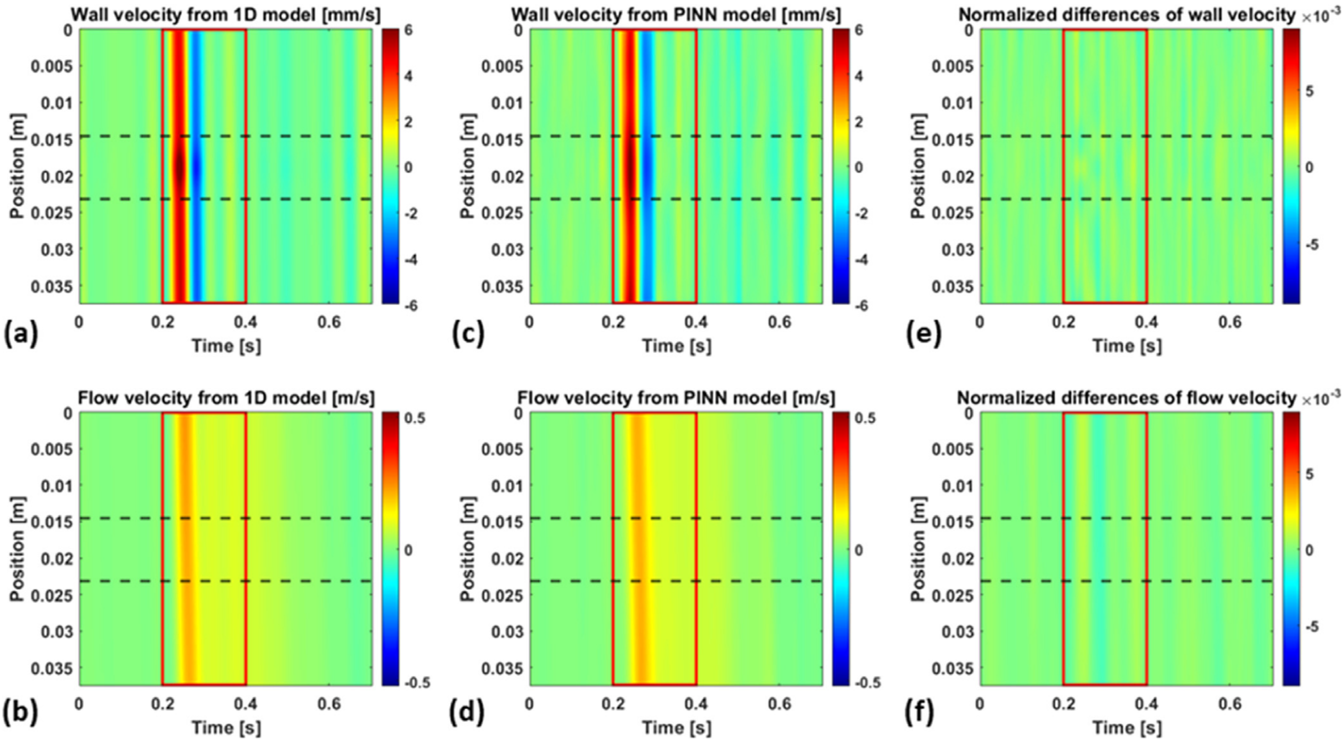

Figure 8. In-silico wall motion and flow velocity for the softer plaque case are shown in (a) and (b), respectively. The corresponding PINN outputs are displayed in (c) and (d). The normalized differences between the in-silico data and the PINN outputs are presented in (e) and (f). The region of interest (marked with a red box) is chosen based on the location of the propagating wave. The maximum differences in the region of interest for wall velocity and flow velocity are 0.12% and 0.11% respectively. The area between the black dashed lines indicates the region where wall softening occurred.

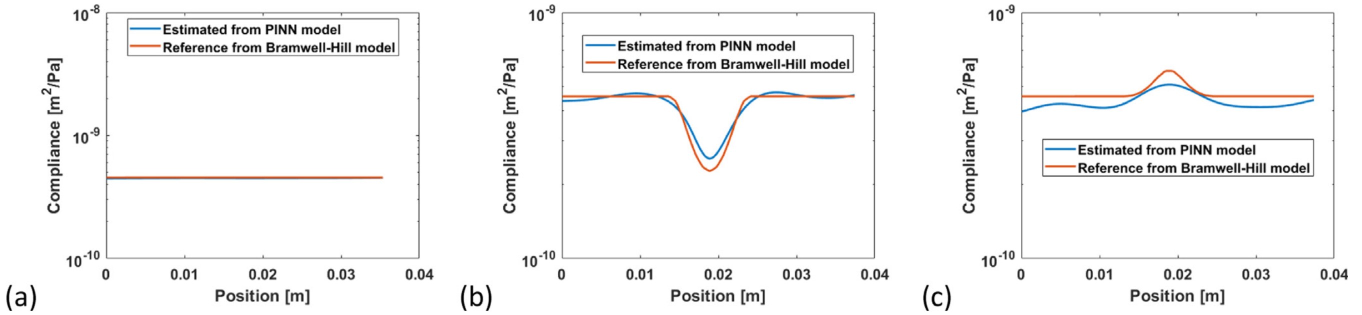

Figure 9. Variations of the compliance corresponding to the (a) homogeneous, (b) stiffer plaque, and (c) softer plaque are shown here. The reference compliance (shown in red color) is obtained using the Bramwell Hill model (equation [4]) on the respective in-silico data. The percentage difference between the estimated and the reference compliance are computed using equation (8) which yields 1.41% in the homogeneous, 3.95% in the stiffer plaque and 8.10% in the softer plaque case. Here note that in equation (8), L2-norm is used to compute the differences which includes the differences in both wall and plaque region together.

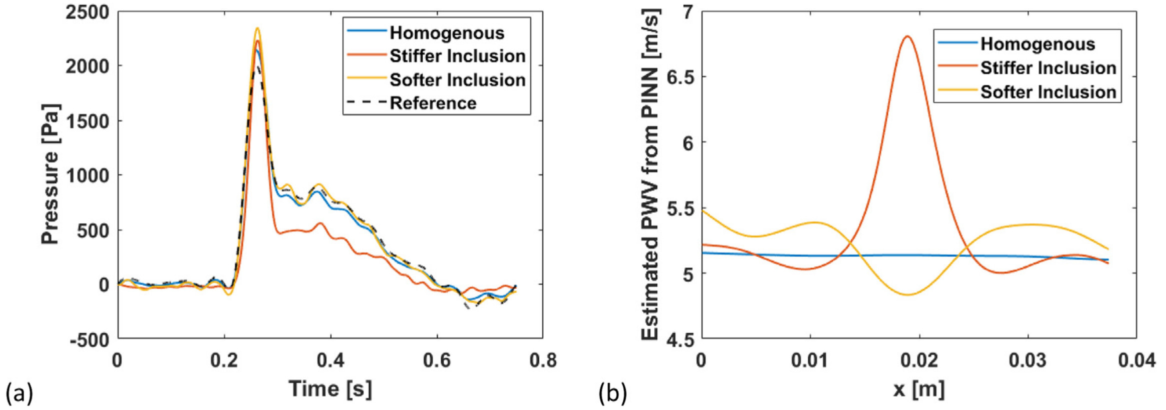

Figure 10. (a) The estimated lumen pressure at the inlet from the proposed PINN model along with the reference inlet pressure that was used to generate the in-silico data are shown here. (b) The resulting estimated pulse wave velocity (PWV) from the PINN model for the in-silico data is presented here. The Bramwell-Hill equation is used to compute PWV from compliance.

model maintains its accuracy and stability across different outlet resistance values, further validating its robustness in various boundary condition scenarios. However, similar to the previous cases, there was a bias of approximately $10^{-10}\ m^2/Pa$ (less than 8%) compared to the reference compliance, as indicated in Figure 15b.

Additionally, we assessed the performance of the proposed inverse model across varying stiffness levels (or compliance). The Young's modulus values considered are illustrated in Figure 16a, while the corresponding compliance outputs from the proposed model are shown in Figure 16b. The model captured the inverse relationship between compliance and Young's modulus, demonstrating lower compliance for higher Young's modulus and vice versa. Also, the model effectively identified localized changes in compliance resulting from variations in Young's modulus. Furthermore, the effect of the plaque length on the performance of the proposed PINN model was studied through considering 6 mm and 10 mm length plaques. The input Young's modulus and the corresponding compliance output from the PINN model for this study are presented in Figure 17 (a and b) respectively. While the model accurately captured the localized length of the plaque, it yielded the combined compliance of the plaque embedded within the vascular wall, which differs from the corresponding point values of the Young's modulus.

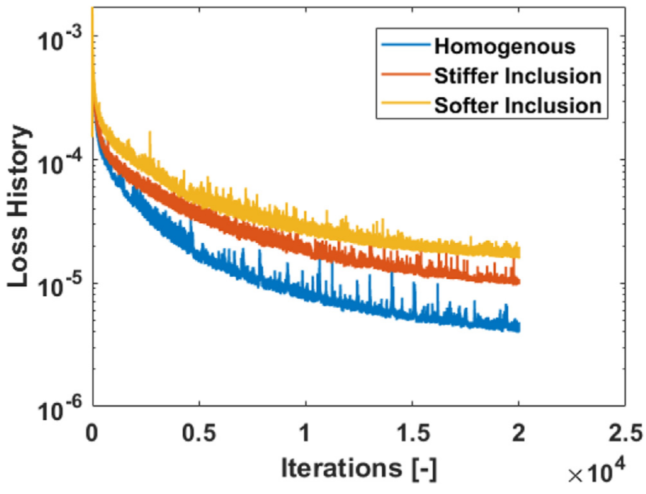

Figure 11. The proposed PINN model's loss history for the three cases in 1D simulated data is shown here.

Phantom study

For the phantom experiment data, we followed the same steps with the PINN model as those used for the 1D simulation data. The results for the phantoms with stiffer and softer plaques are shown in Figure 18 and Figure 19, respectively. Specifically, in both cases, the subplots (a) and (b) show the wall motion and flow velocity of the respective phantoms, the subplots (c) and (d) present the corresponding outputs from the proposed PINN model, while the subplots (e) and (f) display the normalized differences between the measured data from the experiments and the estimated data from the PINN model. In both cases, the percentage difference is within the acceptable limit (0.27% and 1.35% for wall motion and flow velocity, respectively in the region of interest for stiffer plaque case and 0.73% and 1.20% for wall motion and flow velocity, respectively, in the region of interest for softer plaque case). Agreement between the measured data from the experiments and the estimated

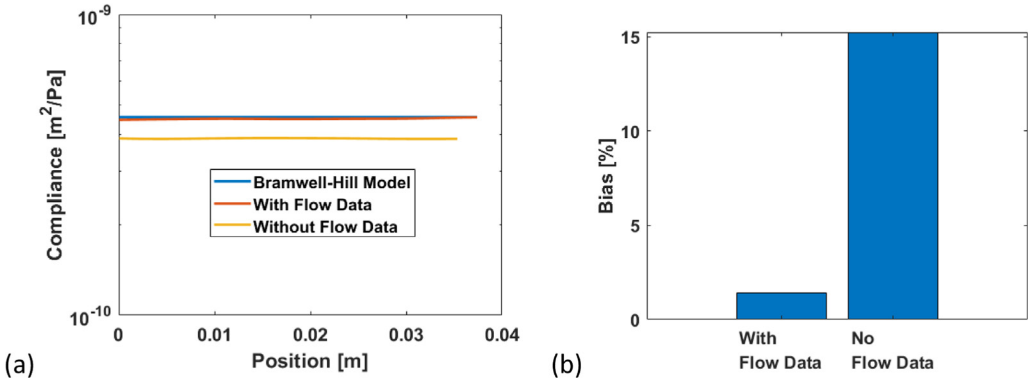

Figure 12. Comparison of compliance variation between cases with and without consideration of fluid flow are shown in (a). The resulting bias in percentage is shown in (b). The reference compliance (shown in blue color in subfigure (a) is obtained using the Bramwell Hill model (equation 4) on the in silico data.

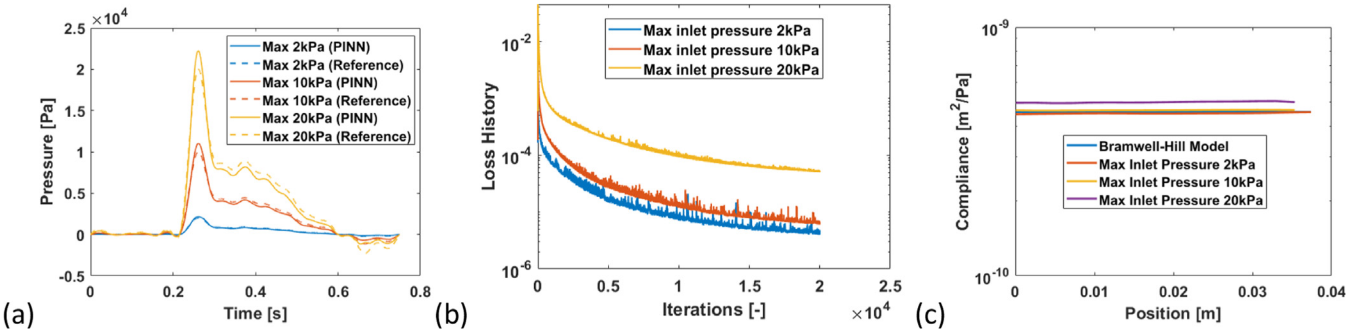

Figure 13. Results for three different inlet pressure cases are shown here. (a) Estimated lumen pressure at the inlet along with the Inlet pressures (reference) used to generate the in-silico data, (b) loss history, and (c) estimated compliance from the proposed PINN model are presented here.

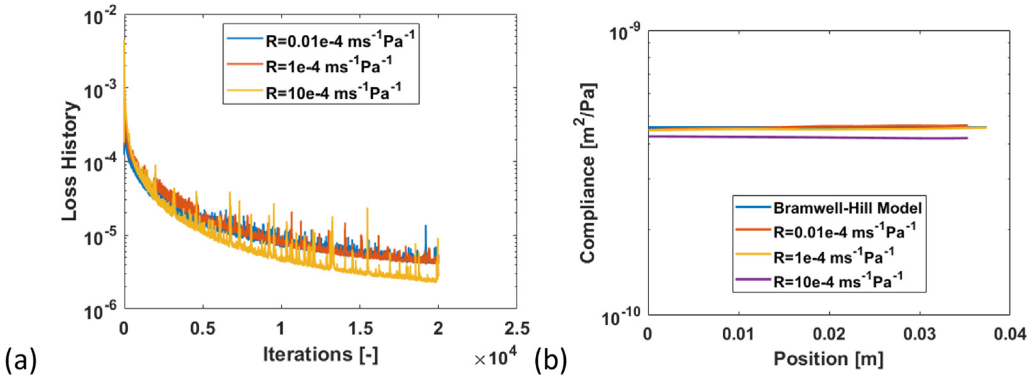

Figure 14. (a) The iteration history and (b) compliance variation corresponding to 3 considered resistance outlet boundary conditions are shown.

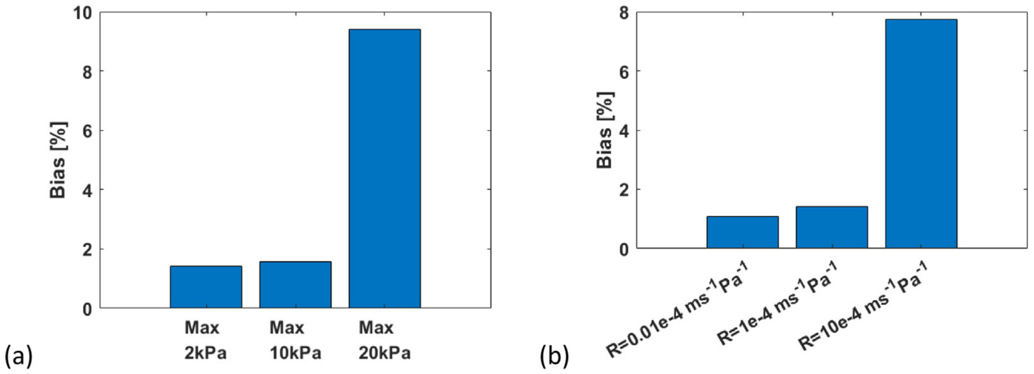

Figure 15. The resulting bias in percentage is presented corresponding to varying inlet pressure (a) and outlet resistance (b) respectively. The reference compliance in both cases is obtained using the Bramwell Hill model (equation 4) on the respective in silico data.

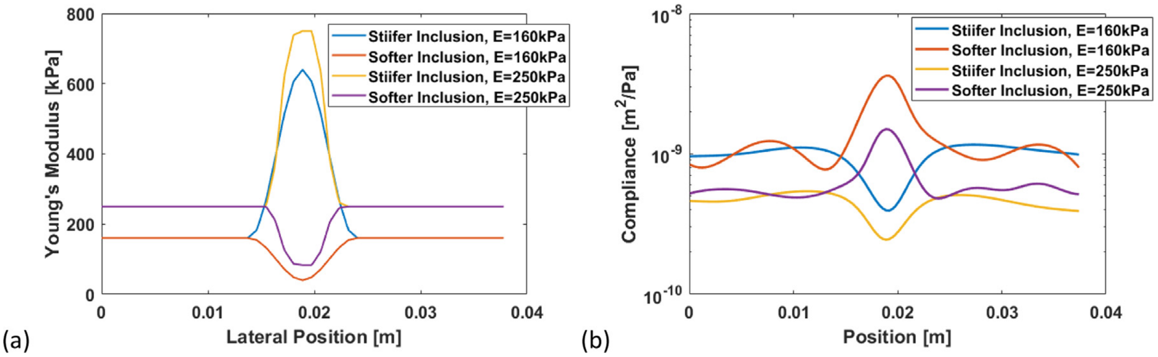

Figure 16. The results from the PINN model illustrating the effects of varying Young's modulus are presented here. (a) displays the Young's modulus values considered in the study, while (b) shows the corresponding output compliance from the proposed PINN model. The model captured the inverse relationship between compliance and Young's modulus, demonstrating lower compliance for higher Young's modulus and vice versa. Additionally, the model effectively identified localized changes in compliance resulting from variations in Young's modulus.

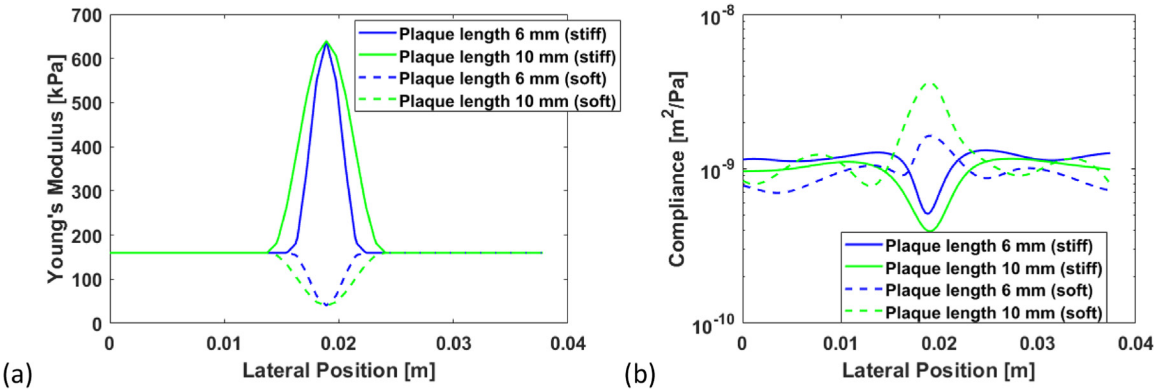

Figure 17. The results from the PINN model illustrating the effects of varying plaque length are presented here. (a) Assigned Young's modulus values considered in the study, (b) Corresponding output compliance from the proposed PINN model. While the model accurately captured the localized length of the plaque, it correctly yielded the combined compliance of the plaque embedded within the vascular wall.

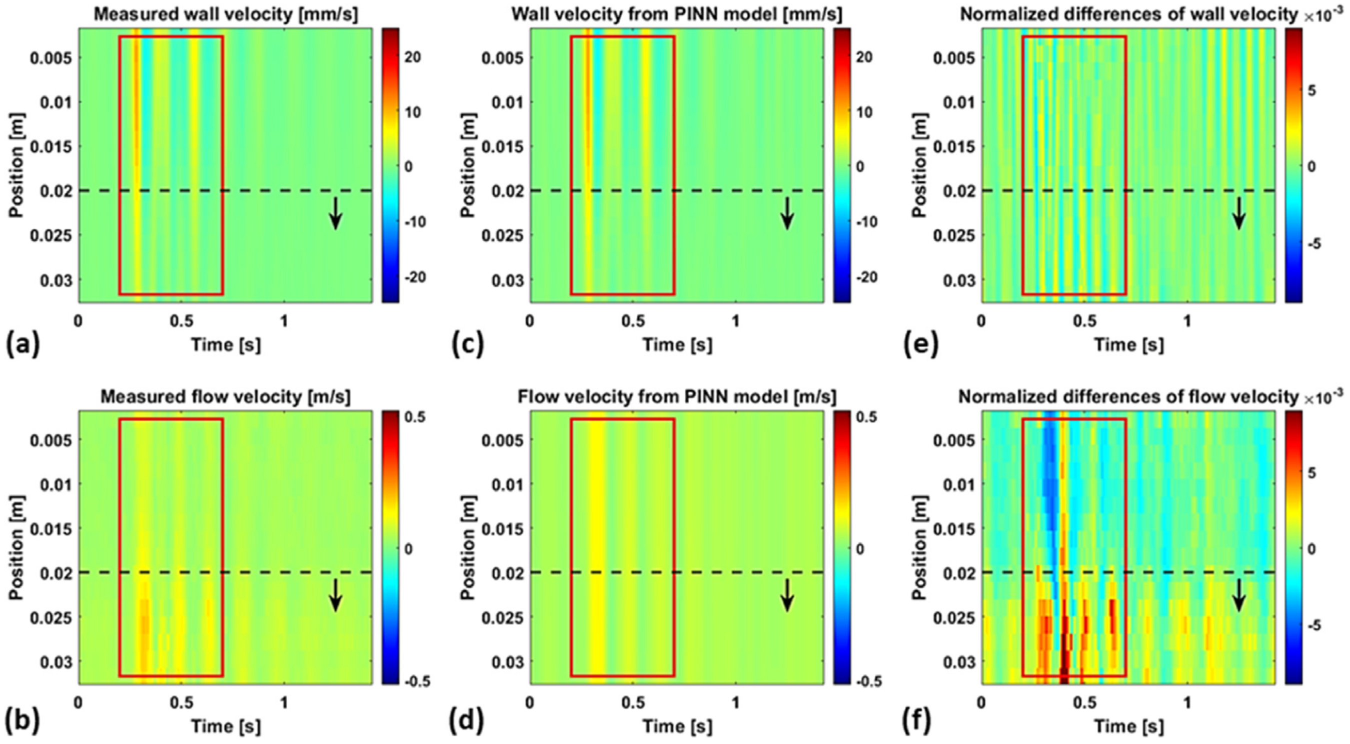

Figure 18. Phantom experiment wall motion and flow velocity for the stiffer plaque case are shown in (a) and (b). The corresponding PINN outputs are displayed in (c) and (d). The normalized differences between the measured data and PINN outputs are presented in (e) and (f). The region of interest (marked with a red box) is chosen based on the location of the propagating wave. The maximum differences in the region of interest for wall velocity and flow velocity are 0.27% and 1.35% respectively. The area marked by the black dashed line and arrow highlights the region containing the stiffer plaque in the phantom setup.

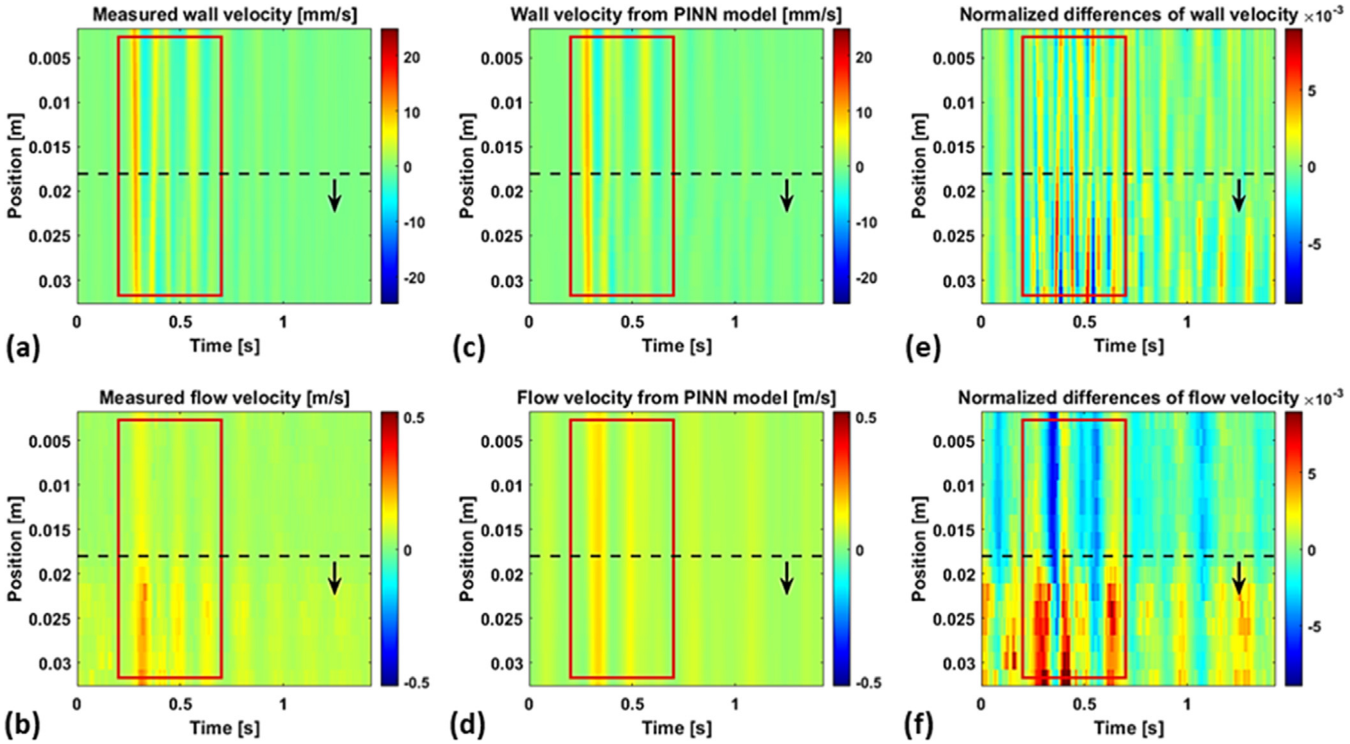

Figure 19. Phantom experiment wall motion and flow velocity for the softer plaque case are shown in (a) and (b). The corresponding PINN outputs are displayed in (c) and (d). The normalized differences between the measured data and PINN outputs are presented in (e) and (f). The region of interest (marked with a red box) is chosen based on the location of the propagating wave. The maximum differences in the region of interest for wall velocity and flow velocity are 0.73% and 1.20% respectively. The area marked by the black dashed line and arrow highlights the region containing the softer plaque in the phantom setup.

data from the proposed PINN model can be further improved with a higher number of iterations.

The resulting estimated PWV for all three cases is shown in Figure 20. As expected, the PWV variation is constant for the non-stenotic region, increases within the plaque region for the stiffer plaque, and decreases within the plaque region for the softer plaque. These results demonstrate the effectiveness of the PINN model in capturing the localized estimated PWV in stenotic phantoms.

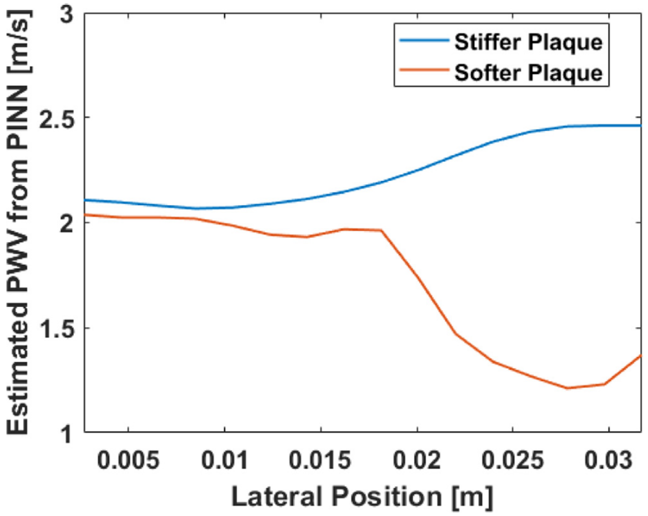

Figure 20. The resulting pulse wave velocity (PWV) from the PINN model for the stenotic phantom experiment data is presented here. The lateral length (range of (x)) corresponds to the same dimensions as those depicted in the B-mode images shown in Figure 5. The post-stenotic region is excluded from this analysis due to the violation of the governing equations caused by the complex flow profile, which includes turbulence.

Table 1 shows the estimated Young's modulus derived from the proposed PINN model alongside the results from uniaxial compression tests. In the PINN model, the Moens-Korteweg equation is utilized to calculate Young's modulus based on the estimated pulse wave velocity. While these results effectively distinguish between stiffer and softer plaque phantoms, it is important to note that the uniaxial compression test results do not provide a direct comparison, as discussed in the Discussion section.

Effect of surrounding material

In this subsection, we present the results regarding the impact of surrounding tissue on the proposed inverse model. Specifically, we conducted two phantom experiments: the first case involved no ultrasound scatterer in the background, the second case included graphite as the ultrasound scatterer. An axial depth of approximately 25 mm was selected for all three phantom cases, as this depth is typically observed

Table 1
Estimated Young's modulus from the proposed PINN model and uniaxial compression test are presented here

Phantom cases	Young's modulus (kPa) Proposed PINN model	Uniaxial compression
Pre-plaque region	13.87	30
Stiffer plaque	20.62	95
Softer plaque	4.75	12

For the results from the PINN model, Moen's Korteweg equation is applied to compute the Young's modulus from the estimated pulse wave velocity. Here note that while these mechanical testing results help us determine whether we have produced stiffer or softer plaque phantoms, it does not provide a direct one-to-one comparison, as the stiffness of the embedded plaque within a different stiffness wall will differ from the uniaxial mechanical testing of a single material cube specimen.

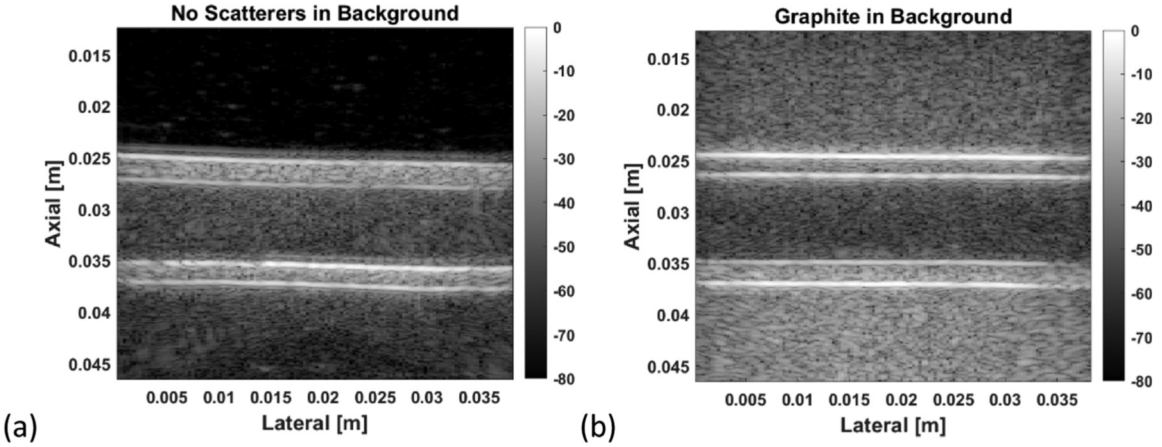

Figure 21. B-mode images of the phantom setups used to study the effect of surrounding tissue. (a) displays the case without any scatterer in the gelatin background, while (b) illustrates the case with graphite as ultrasound scatterers inside the gelatin background.

in vivo in common carotid artery assessments [56]. The B-mode images from these experiments are shown in Figure 21, highlighting the presence of scatterers (higher echogenicity) in the graphite case (Figure 21b) compared to the no-scatterer case (Figure 21a). The corresponding PINN outputs are presented in Figure 22, where the resulting compliances are found to be quite similar. The small discrepancies observed are attributed to the variability inherent in the PVA phantom manufacturing process used in this study.

Discussion

In this study, we propose a PINN-based inverse approach for estimating localized pulse wave velocity, particularly in arteries with atherosclerotic plaques. Our approach leverages both wall motion and fluid flow data obtained from PWI and VFI pipelines, respectively. The governing 1D differential equations, as outlined in the equations (1) to (3), are incorporated into the PINN framework to ensure the model adheres to the underlying physics. The proposed method was validated using 1D simulation results and its performance was further assessed with artery-mimicking phantoms.

For the straight homogeneous system, 1D simulation studies showed that the percentage difference between the PINN outputs and the reference quantities is smaller compared to the heterogeneous cases with either stiffer or softer plaques. This observation is also reflected in the loss history plot (Figure 11) as well as the resulting bias in the compliance estimation. The increased discrepancy in heterogeneous cases is primarily due to the violation of the assumptions in the underlying differential equations. This violation arises due to the reflection effects from the changes in material and geometric properties due to the presence of plaques. Although we set a high number of iterations to achieve acceptable wall motion and flow velocity results, convergence is slower due to the simplified governing differential equations used in the PINN model. In addition to the compliance, the lumen pressure over the cardiac cycle at the inlet from the proposed PINN model was compared with the reference inlet pressure that was used to generate the in-silico data (Fig. 10a). Here also, the estimated lumen pressure is close to the reference value. The resulting pulse wave velocity are presented in Figure 10b indicating the localized changes in the heterogenous cases according to its stiffness.

The effect of incorporating flow data was examined in Figure 12. As expected, including flow data enabled the proposed inverse model to converge to compliance values closer (13.84% more) to the reference values, which were computed using Bramwell-Hill equation (4) for known geometric and material properties. To demonstrate the robustness of the proposed inverse model with respect to inlet and outlet boundary conditions, we varied the magnitude of the inlet pressure and the resistance at the outlet boundary (Fig. 13 and Fig. 14). While a bias ($\approx 10^{-10}\ m^2/Pa$ (less than 10%)) effect was observed, the model successfully converged to the reference compliance and lumen pressure value at the inlet within the considered ranges of these boundary conditions. Additionally, we investigated the performance of the proposed inverse model with varying stiffness and plaque length, as presented in Figure 16 and Figure 17 respectively. Our observations indicate that the estimated compliance aligns with the corresponding Young's modulus variation. However, the model yielded the combined compliance of the plaque embedded within the vascular wall, which differed from the corresponding point values of Young's modulus.

The proposed model effectively captured localized changes in compliance and pulse wave velocity, as illustrated in Figure 9 and Figure 10 respectively for the 1D simulated data. The observed biases in compliance estimation when compared with the Bramwell-Hill equation are 1.41% for the homogenous case, 3.95% for the stiffer plaque, and 8.10% for the softer plaque in the simulation cases. The reader should note that the underlying assumptions of the Bramwell-Hill equations are violated in the case of a stenotic artery. Additionally, we have errors in which the underlying partial differential equations (PDEs) are solved; specifically, we did not utilize the boundary conditions as typically required in standard PDE solutions.

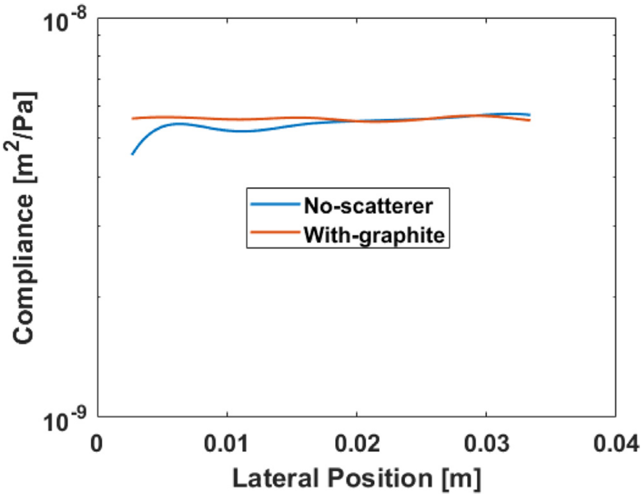

Figure 22. Variation in compliance resulting from the proposed PINN model for the two phantom setups: one case without any scatterers in the background gelatin and the other case featuring graphite as background scatterers are presented here.

Furthermore, in heterogeneous cases, deviations from the assumptions inherent in the linearized version of the PDEs contribute to inaccuracies. Consequently, all these factors led to biases in the resulting compliance estimations in both stenotic and non-stenotic regions. Additionally, we observed a higher bias in the compliance values for the softer plaque cases compared to the stiffer plaque cases in our current PINN framework consistently across all the cases considered. The underlying reasons for this higher bias are not fully understood at this stage and warrant further investigation in future studies.

In the phantom studies, the model captured the localized changes in pulse wave velocity, as illustrated in Figure 20. However, this work primarily focused on the pre-plaque and plaque regions in the phantom studies to avoid the complexities associated with vortex formation and other intricate flow profiles present in the post-plaque region, which could violate the inherent assumptions of the governing PDEs. Incorporating these complex flow profiles will be feasible when extending the PINN model from 1D to 2D or 3D, with the corresponding adjustments to the neural network architecture. Future research that combines 3D fluid-structure interaction simulations with successive Field-II simulations could be particularly useful in verifying such a higher-dimensional PINN model.

Additionally, the estimated Young's modulus derived from the proposed PINN model are compared with the corresponding uniaxial compression test results in Table 1. We should note that the mechanical testing method employed in this study yields the Young's modulus of the cube specimens formed at the same time as the arterial phantoms used in the study. While these mechanical testing results help us determine whether we have produced stiffer or softer plaque phantoms, they do not provide a direct one-to-one mapping, as the stiffness of the embedded plaque within a wall of distinct stiffness will differ from the uniaxial mechanical testing of a single material cube specimen.

Furthermore, in the phantom study, we examined the effect of surrounding tissue by incorporating ultrasound scatterers into the background gelatin. As shown in Figure 22, the resulting compliance value for the case with graphite in the background gelatin is quite similar to the no background scatterer case. Although the presence of ultrasound scatterers introduces aberration effects, the characteristic shapes of wall motion and flow velocity remained consistent in between these two cases. This consistency can be attributed to the relatively shallow axial depth of approximately 25 mm, which reflects typical *in vivo* conditions in the common carotid artery. Consequently, even though the proposed PINN model did not account for background tissue information, it converged to similar compliance values for both scatterer and no scatterer cases. The small discrepancies observed in Figure 22 couldbe attributed in part to the variability inherent in the PVA phantom manufacturing process used in this study. Another observation to note is the slightly increased echogenicity detected in the posterior background compared to the anterior background, as shown in the B-mode images of Figure 21. This disparity is attributed to artifacts arising from ultrasound beamforming and multiple reflections stemming from the bottom and sides of the phantom setup.

In terms of computational time, the specified 20,000 iterations took less than 1 hour to complete on an NVIDIA GPU Quadro RTX 5000. Future work will focus on adjusting the number of iterations based on problem convergence to reduce computational time for simpler geometries and material properties. Additionally, GPU memory allocation for allowing the entire space-time data from the experiment in the proposed model was challenging even when solving a 1D pulse wave propagation problem. Currently, we addressed this through temporal truncation and focused only on the single wave propagation region. In future studies, we will optimize the model to work at sufficiently low framerate without jeopardizing sampling for PWI and VFI while allowing reduction of the computational time and potentially permitting real-time applications at multiple cardiac cycles. In this regard, we will also look into the use of various recently implemented solver for inverse problems such as Optimizing a DIscrete Loss (ODIL) [57] and others for this application to reduce the computational time for the real time implementation.

This study considered the linearized version of the governing equations; however, incorporating nonlinearity will be more applicable for arteries with plaques and will be addressed in future research. Furthermore, arterial walls exhibit viscoelastic properties; however, this study did not account for the viscosity term. In future version of the model, we plan to investigate viscoelasticity by incorporating the relevant term into the governing equations and then validating with the respective viscoelastic phantoms. In this regard, we also plan to enhance our phantom setup by utilizing different materials and/or higher concentration PVA along with the higher number of freeze-thaw cycles to better replicate the stiffness characteristics of the human common carotid artery tissue (in the current phantom setup, we observed pulse wave velocity of 2 m/s while the observed pulse wave velocity is 4 m/s for *in vivo* human common carotid arteries in healthy cohorts). Additionally, adaptive weight terms will be explored to replace the manually adjusted weights used in this study, consistent with the numerical orders of each term in the loss function (equation *5*). When additional information related to inlet and outlet boundary conditions is available, it can be incorporated into the loss function to facilitate more accurate convergence.

Conclusion

This study demonstrated the potential of a novel PINN-based inverse approach for estimating localized wall compliance, particularly in arteries with plaques. We leveraged both wall motion and fluid flow velocities obtained from PWI and VFI pipelines, respectively, and incorporated the governing 1D differential equations into the PINN framework to adhere the model to the underlying physics. The proposed method was validated through 1D simulations and further assessed using artery-mimicking phantoms, demonstrating its feasibility for *in vivo* applications. The results presented showed that the proposed PINN model effectively captures localized changes in compliance and pulse wave velocity across different scenarios, including homogeneous geometries but also bearing stiffer and softer plaques. The model's robustness was further validated by its ability to handle varying inlet pressure and resistance boundary conditions, maintaining accuracy within acceptable limits. Additionally, the inclusion of flow data improved the model's convergence to compliance values closer to the reference values. The proposed inverse approach thus offers a promising avenue for non-invasive assessment of arterial health, with future extensions to incorporating non-linearity into the governing equations and extending to 2D or 3D models expected to further enhance its clinical utility.

Data statement

The data supporting the findings of this study will be made available upon request. Please contact the corresponding author for access to the datasets used in this research.

Conflict of interest

The authors declare that there are no conflicts of interest related to this manuscript. Additionally, we confirm that this study did not involve any human or animal subjects. All research was conducted using computational simulations and phantom experiments, ensuring compliance with ethical standards.

Acknowledgments

The study was funded by the National Institutes of Health: NIH R01HL167085-01A1. The content is solely the responsibility of the authors and does not necessarily represent the official views of the National Heart, Lung, and Blood Institute or the National Institutes of

Health. The authors thank Pengcheng (Cosima) Liang, MS, and Parth Gami, MS for their support.

References

[1] Baradaran H, Gupta A. Carotid artery stiffness: imaging techniques and impact on cerebrovascular disease. Front Cardiovasc Med 2022;9:852173. doi: 10.3389/FCVM.2022.852173.

[2] Pewowaruk RJ, Korcarz C, Stein JH, Bluemke D, Tedla Y, Gepner AD. Methods of arterial stiffness calculation and cardiovascular disease events: the multi-ethnic study of atherosclerosis (MESA). J Hypertens 2023;41:486. doi: 10.1097/HJH.0000000000003365.

[3] Westenberg JJM, Van Poelgeest EP, Steendijk P, Grotenhuis HB, Jukema JW, De Roos A. Bramwell-Hill modeling for local aortic pulse wave velocity estimation: a validation study with velocity-encoded cardiovascular magnetic resonance and invasive pressure assessment. J Cardiovasc Magnetic Resonance 2012;14:15. doi: 10.1186/1532-429X-14-2.

[4] Tomiyama H, Yamashina A, Arai T, Hirose K, Koji Y, Chikamori T, et al. Influences of age and gender on results of noninvasive brachial−ankle pulse wave velocity measurement—a survey of 12517 subjects. Atherosclerosis 2003;166:303–9. doi: 10.1016/S0021-9150(02)00332-5.

[5] Chen CH, Nevo E, Fetics B, Pak PH, Yin FCP, Maughan WL, et al. Estimation of central aortic pressure waveform by mathematical transformation of radial tonometry pressure: validation of generalized transfer function. Circulation 1997;95:1827–36. doi: 10.1161/01.CIR.95.7.1827.

[6] Horie N, Morikawa M, Ishizaka S, Takeshita T, So G, Hayashi K, et al. Assessment of carotid plaque stability based on the dynamic enhancement pattern in plaque components with multidetector CT angiography. Stroke 2012;43:393–8. doi: 10.1161/STROKEAHA.111.635953.

[7] Freilinger TM, Schindler A, Schmidt C, Grimm J, Cyran C, Schwarz F, et al. Prevalence of nonstenosing, complicated atherosclerotic plaques in cryptogenic stroke. JACC Cardiovasc Imaging 2012;5:397–405. doi: 10.1016/j.jcmg.2012.01.012.

[8] Brinjikji W, Rabinstein AA, Lanzino G, Murad MH, Williamson EE, DeMarco JK, et al. Ultrasound characteristics of symptomatic carotid plaques: a systematic review and meta-analysis. Cerebrovasc Dis 2015;40:165–74. doi: 10.1159/000437339.

[9] Coolen BF, Poot DHJ, Liem MI, Smits LP, Gao S, Kotek G, et al. Three-dimensional quantitative T1 and T2 mapping of the carotid artery: sequence design and in vivo feasibility, Wiley Online Library BF Coolen, DHJ Poot, MI Liem, LP Smits, S Gao, G Kotek, S Klein, AJ NederveenMagnetic Resonance in Medicine. 2016•Wiley Online Library 2016;75:1008–17. doi: 10.1002/MRM.25634.

[10] Wang G, Atef M, Lian Y. Towards a continuous non-invasive cuffless blood pressure monitoring system using PPG: systems and circuits review. IEEE Circuits and Systems Magazine 2018;18:6–26. doi: 10.1109/MCAS.2018.2849261.

[11] Rodriguez-Labra JI, Kosik C, Maddipatla Di, Narakathu BB, Atashbar MZ. Development of a PPG sensor array as a wearable device for monitoring cardiovascular metrics. IEEE Sens J 2021;21:26320–7. doi: 10.1109/JSEN.2021.3064219.

[12] Pruijssen JT, de Korte CL, Voss I, Hansen HHG. Vascular shear wave elastography in atherosclerotic arteries: a systematic review. Ultrasound Med Biol 2020;46:2145–63. doi: 10.1016/J.ULTRASMEDBIO.2020.05.013.

[13] Sarvazyan AP, Rudenko OV, Swanson SD, Fowlkes JB, Emelianov SY. Shear wave elasticity imaging: a new ultrasonic technology of medical diagnostics. Ultrasound Med Biol 1998;24:1419–35. doi: 10.1016/S0301-5629(98)00110-0.

[14] Roy T, Lee HK, Capron CB, Lopez-Jimenez F, Hesley GK, Greenleaf JF, et al. Estimation of in vivo human carotid artery elasticity using arterial dispersion ultrasound vibrometry. Ultrasound Med Biol 2025;51:250–61. doi: 10.1016/J.ULTRASMEDBIO.2024.09.023.

[15] Couade M, Pernot M, Prada C, Messas E, Emmerich J, Bruneval P, et al. Quantitative assessment of arterial wall biomechanical properties using shear wave imaging. Ultrasound Med Biol 2010;36:1662–76. doi: 10.1016/j.ultrasmedbio.2010.07.004.

[16] Goudot G, Sitruk J, Jimenez A, Julia P, Khider L, Alsac JM, et al. Carotid plaque vulnerability assessed by combined shear wave elastography and ultrafast doppler compared to histology. Transl Stroke Res 2022;13:100–11. doi: 10.1007/S12975-021-00920-6.

[17] Marlevi D, Mulvagh SL, Huang R, DeMarco JKevin, Ota H, Huston J, et al. Combined spatiotemporal and frequency-dependent shear wave elastography enables detection of vulnerable carotid plaques as validated by MRI. Sci Rep 2020;10:1–13. doi: 10.1038/S41598-019-57317-7.

[18] Lou Z, Yang J, Tang L, Jin Y, Zhang J, Liu C, Li Q. Shear wave elastography imaging for the features of symptomatic carotid plaques: a feasibility study. J Ultrasound Med 2017;36:1213–23. doi: 10.7863/ULTRA.16.04073.

[19] Anand KS, Torres G, Homeister JW, Caughey MC, Gallippi CM. Comparing focused-tracked and plane wave-tracked ARFI Log(VoA) in silico and in application to human carotid atherosclerotic plaque, ex vivo. IEEE Trans Ultrason Ferroelectr Freq Control 2023;70:636–52. doi: 10.1109/TUFFC.2023.3278495.

[20] Roy-Cardinal MH, Destrempes F, Soulez G, Cloutier G. Assessment of carotid artery plaque components with machine learning classification using homodyned-k parametric maps and elastograms. IEEE Trans Ultrason Ferroelectr Freq Control 2019;66:493–504. doi: 10.1109/TUFFC.2018.2851846.

[21] De Korte CL, Pasterkamp G, Van Der Steen AFW, Woutman HA, Bom N. Characterization of plaque components with intravascular ultrasound elastography in human femoral and coronary arteries in vitro. Circulation 2000;102:617–23. doi: 10.1161/01.CIR.102.6.617.

[22] Baldewsing RA, Schaar JA, Mastik F, Oomens CWJ, Van Der Steen AFW. Assessment of vulnerable plaque composition by matching the deformation of a parametric plaque model to measured plaque deformation. IEEE Trans Med Imaging 2005;24:514–28. doi: 10.1109/TMI.2005.844170.

[23] Schaar JA, van der Steen AFW, Mastik F, Baldewsing RA, Serruys PW. Intravascular palpography for vulnerable plaque assessment. J Am Coll Cardiol 2006;47. doi: 10.1016/J.JACC.2006.01.035.

[24] Nauleau P, Apostolakis I, McGarry M, Konofagou E. Cross-correlation analysis of pulse wave propagation in arteries: in vitro validation and in vivo feasibility. Phys Med Biol 2018;63:115006. doi: 10.1088/1361-6560/AABE57.

[25] Apostolakis I-Z, Nauleau P, Papadacci C, Mcgarry MD, Konofagou EE. Feasibility and validation of 4-D pulse wave imaging in phantoms and in vivo. IEEE Trans Ultrason Ferroelectr Freq Control 2017;64. doi: 10.1109/TUFFC.2017.2735381.

[26] Apostolakis IZ, Mcgarry MDJ, Bunting EA, Konofagou EE. Pulse wave imaging using coherent compounding in a phantom and in vivo. Phys Med Biol 2017;62:1700. doi: 10.1088/1361-6560/AA553A.

[27] Fujikura K, Luo J, Gamarnik V, Pernot M, Fukumoto R, Tilson MD, et al. A novel noninvasive technique for pulse-wave imaging and characterization of clinically-significant vascular mechanical properties in vivo. Ultrason Imaging 2007;29:137–54. doi: 10.1177/016173460702900301.

[28] Luo J, Fujikura K, Tyrie LS, Tilson MD, Konofagou EE. Pulse wave imaging of normal and aneurysmal abdominal aortas in vivo. IEEE Trans Med Imaging 2009;28:477–86. doi: 10.1109/TMI.2008.928179.

[29] Li RX, Luo J, Balaram SK, Chaudhry FA, Shahmirzadi D, Konofagou EE. Pulse wave imaging in normal, hypertensive and aneurysmal human aortas in vivo: a feasibility study. Phys Med Biol 2013;58:4549. doi: 10.1088/0031-9155/58/13/4549.

[30] Luo J, Li RX, Konofagou EE. Pulse wave imaging of the human carotid artery: An in vivo feasibility study. IEEE Trans Ultrason Ferroelectr Freq Control 2012;59:174–81. doi: 10.1109/TUFFC.2012.2170.

[31] Mobadersany N, Liang P, Kemper P, Konofagou EE. Polyvinyl alcohol phantoms with heterogeneous plaques: estimation of pulse wave velocity at the stenotic region using pulse wave imaging. Ultrasound Med Biol 2024;50:91–8. doi: 10.1016/j.ultrasmedbio.2023.09.005.

[32] Mobadersany N, Meshram NH, Kemper P, Sise CV, Karageorgos GM, Liang P, et al. Pulse wave imaging of a stenotic artery model with plaque constituents of different stiffnesses: experimental demonstration in phantoms and fluid-structure interaction simulation. J Biomech 2023;149:111502. doi: 10.1016/j.jbiomech.2023.111502.

[33] Karageorgos GM, Kemper P, Lee C, Weber R, Kwon N, Meshram N, et al. Adaptive wall shear stress imaging in phantoms, simulations and in vivo. IEEE Trans Biomed Eng 2023;70:154–65. doi: 10.1109/TBME.2022.3186854.

[34] Karageorgos GM, Apostolakis IZ, Nauleau P, Gatti V, Weber R, Kemper P, et al. Pulse wave imaging coupled with vector flow mapping: a phantom, simulation, and in vivo study. IEEE Trans Ultrason Ferroelectr Freq Control 2021;68:2516–31. doi: 10.1109/TUFFC.2021.3074113.

[35] Afrakhteh S, Demi L. Mitigating high frame rate demands in shear wave elastography using radial basis function-based reconstruction: An experimental phantom study. Ultrasonics 2025;148:107542. doi: 10.1016/J.ULTRAS.2024.107542.

[36] Afrakhteh S, Iacca G, Demi L. High frame rate ultrasound imaging by means of tensor completion: application to echocardiography. IEEE Trans Ultrason Ferroelectr Freq Control 2023;70:41–51. doi: 10.1109/TUFFC.2022.3223499.

[37] Afrakhteh S, Behnam H. Coherent plane wave compounding combined with tensor completion applied for ultrafast imaging. IEEE Trans Ultrason Ferroelectr Freq Control 2021;68:3094–103. doi: 10.1109/TUFFC.2021.3087504.

[38] Goudarzi S, Basarab A, Rivaz H. Inverse problem of ultrasound beamforming with denoising-based regularized solutions. IEEE Trans Ultrason Ferroelectr Freq Control 2022;69:2906–16. doi: 10.1109/TUFFC.2022.3198874.

[39] Goudarzi S, Basarab A, Rivaz H. A unifying approach to inverse problems of ultrasound beamforming and deconvolution. IEEE Trans Comput Imaging 2023;9:197–209. doi: 10.1109/TCI.2023.3248945.

[40] Doyley MM. Model-based elastography: a survey of approaches to the inverse elasticity problem. Phys Med Biol 2012;57:R35. doi: 10.1088/0031-9155/57/3/R35.

[41] Mcgarry M, Li R, Apostolakis I, Nauleau P, Konofagou EE. An inverse approach to determining spatially varying arterial compliance using ultrasound imaging, Physics in Medicine & Biology Institute of Physics and Engineering in Medicine. Phys Med Biol 2016;61:5486–507. doi: 10.1088/0031-9155/61/15/5486.

[42] Korteweg DJ. Ueber die Fortpflanzungsgeschwindigkeit des Schalles in elastischen Röhren. Annalen der Physik und Chemie, New Series, 5; 1878. p. 1878525–42.

[43] Shahmirzadi D, Konofagou EE. Detection of aortic wall inclusions using regional pulse wave propagation and velocity in silico. Artery Res 2012;6:114–23. doi: 10.1016/J.ARTRES.2012.05.004.

[44] McGarry M, Nauleau P, Apostolakis I, Konofagou E. In vivo repeatability of the pulse wave inverse problem in human carotid arteries. J Biomech 2017;64:136–44. doi: 10.1016/J.JBIOMECH.2017.09.017.

[45] Kemper P, Mobadersany N, Konofagou EE. Robust localized stiffness assessment by combining flow and wall motion using a 1-D wave propagation model. IEEE International Ultrasonics Symposium, IUS 2022-Octob; 2022. doi: 10.1109/IUS54386.2022.9957795.

[46] Kemper P. High frame-rate pulse wave imaging for non-invasive characterization of arterial stiffness in vivo. PhD dissertation Columbia University; 2023.

[47] Liang P, Kemper P, Konofagou EE. A physics-informed neural network approach to the pulse wave inverse problem for noninvasive intravascular pressure estimate. IEEE International Ultrasonics Symposium, IUS; 2023. doi: 10.1109/IUS51837.2023.10308234.

[48] Roy T, Kemper P, Mobadersany N, Konofagou EE. A physics-informed neural network approach for determining spatially varying arterial stiffness using ultrasound imaging: Finite Difference simulation and experimental plaque phantom validation.

IEEE Ultrasonics, Ferroelectrics, and Frequency Control Joint Symposium, UFFC-JS 2024 - Proceedings; 2024. doi: 10.1109/UFFC-JS60046.2024.10794027.

[49] Vlachopoulos C, O'Rourke M, Nichols WW. McDonald's blood flow in arteries : theoretical, experimental and clinical principles. McDonald's Blood Flow in Arteries 2011. doi: 10.1201/B13568.

[50] Gami P, Kemper P, Karageorgos G, Swingle T, Webber R, Konofagou EE. Characterization of nonlinear elasticity of the carotid artery using pulse wave imaging: a feasibility study in hypertensive and carotid artery disease patients in vivo. IEEE International Ultrasonics Symposium, IUS 2022-Octob; 2022. p. 1–4. doi: 10.1109/IUS54386.2022.9957838.

[51] Teng Z, Zhang Y, Huang Y, Feng J, Yuan J, Lu Q, et al. Material properties of components in human carotid atherosclerotic plaques: a uniaxial extension study. Acta Biomater 2014;10:5055–63. doi: 10.1016/J.ACTBIO.2014.09.001.

[52] Holdsworth DW, Norley CJD, Frayne R, Steinman DA, Rutt BK. Characterization of common carotid artery blood-flow waveforms in normal human subjects. Physiol Meas 1999;20:219–40. doi: 10.1088/0967-3334/20/3/301.

[53] Apostolakis IZ, Mcgarry MDJ, Bunting EA, Konofagou EE. Pulse wave imaging using coherent compounding in a phantom and in vivo. Phys Med Biol 2017;62:1700. doi: 10.1088/1361-6560/AA553A.

[54] Kemper PPN, Mahmoudi S, Apostolakis IZ, Konofagou EE. Feasibility of bi-linear mechanical characterization of the abdominal aorta in a hypertensive mouse model. Ultrasound Med Biol 2021;47:3480. doi: 10.1016/J.ULTRASMEDBIO.2021.08.001.

[55] Baranger J, Arnal B, Perren F, Baud O, Tanter M, Demene C. Adaptive spatiotemporal SVD clutter filtering for ultrafast doppler imaging using similarity of spatial singular vectors. IEEE Trans Med Imaging 2018;37:1574–86. doi: 10.1109/TMI.2018.2789499.

[56] Tommasin D, Caenen A, Verhegghe B, Greenwald S, Segers P. Physics of within-tissue wave propagation generated by pulse propagation in the carotid artery. Appl Sci 2019 2019;9:2878. Page 2878 9. doi: 10.3390/APP9142878.

[57] Karnakov P, Litvinov S, Koumoutsakos P. Solving inverse problems in physics by optimizing a discrete loss: Fast and accurate learning without neural networks. PNAS Nexus 2024;3. doi: 10.1093/PNASNEXUS/PGAE005.